Sea Surface Temperature Patterns on the West Florida Shelf Using Growing Hierarchical Self-Organizing Maps

YONGGANG LIU AND ROBERT H. WEISBERG

College of Marine Science, University of South Florida, St. Petersburg, Florida

RUOYING HE

Woods Hole Oceanographic Institution, Woods Hole, Massachusetts

(Manuscript received 10 September 2004, in final form 23 March 2005)

ABSTRACT

Neural network analyses based on the self-organizing map (SOM) and the growing hierarchical self-organizing map (GHSOM) are used to examine patterns of the sea surface temperature (SST) variability on the West Florida Shelf from time series of daily SST maps from 1998 to 2002. Four characteristic SST patterns are extracted in the first-layer GHSOM array: winter and summer season patterns, and two transitional patterns. Three of them are further expanded in the second layer, yielding more detailed structures in these seasons. The winter pattern is one of low SST, with isotherms aligned approximately along isobaths. The summer pattern is one of high SST distributed in a horizontally uniform manner. The spring transition includes a midshelf cold tongue. Similar analyses performed on SST anomaly data provide further details of these seasonally varying patterns. It is demonstrated that the GHSOM analysis is more effective in extracting the inherent SST patterns than the widely used EOF method. The underlying patterns in a dataset can be visualized in the SOM array in the same form as the original data, while they can only be expressed in anomaly form in the EOF analysis. Some important features, such as asymmetric SST anomaly patterns of winter/summer and cold/warm tongues, can be revealed by the SOM array but cannot be identified in the lowest mode EOF patterns. Also, unlike the EOF or SOM techniques, the hierarchical structure in the input data can be extracted by the GHSOM analysis.

1. Introduction

The West Florida Shelf (WFS) is a broad, gently sloping continental margin influenced by the Gulf of Mexico Loop Current system located seaward of the shelf break (Molinari et al. 1977; Huh et al. 1981; Paluszkiewicz et al. 1983; He and Weisberg 2003; Weisberg and He 2003) and by local wind and buoyancy forcing, including the fresh water of the Mississippi River generally found at midshelf in spring and summer (Gilbes et al. 1996; He and Weisberg 2002). The shelf circulation is dynamically linked to its varying water properties, and particularly to temperature, which exerts a primary control on density. The close relationship between the shelf water temperature variability and the variability of net surface heat flux and ocean circulation are reported in recent studies (He and Weisberg 2002, 2003; Weisberg and He 2003; Liu and Weisberg 2005a). Thus, a description of the characteristic patterns of SST variability adds to our understanding of the shelf circulation and its air–sea interactions (Weisberg et al. 2004).

a. Self-organizing map and its applications in meteorology and oceanography

Techniques for pattern detection in large oceanographic datasets are becoming increasingly important as datasets grow in size and complexity. The self-organizing map (SOM), an artificial neural network based on unsupervised learning, is an effective software tool of feature extraction (Kohonen 1982, 2001). It provides a nonlinear cluster analysis, mapping high-dimensional data onto a (usually) 2D output space while preserving the topological relationships between the input data. As a tool of pattern recognition and

Corresponding author address: Robert H. Weisberg, College of Marine Science, University of South Florida, 140 Seventh Avenue South, St. Petersburg, FL 33701.
E-mail: weisberg@marine.usf.edu

classification, the SOM analysis is in widespread use across a number of disciplines (Kaski et al. 1998; Oja et al. 2003). Since its first use in climate research by Hewitson and Crane (1994), extensive applications of the SOM technique have been found in the meteorological community (Malmgren and Winter 1999; Cavazos 1999, 2000; Ambroise et al. 2000; Cavazos et al. 2002; Hewitson and Crane 2002; Hsu et al. 2002; Hong et al. 2004). Recently, the SOM analysis has also been applied in oceanography. For example, Ainsworth (1999) and Ainsworth and Jones (1999) used this method to improve chlorophyll estimates from satellite data. Silulwane et al. (2001) and Richardson et al. (2002) used it to identify characteristic chlorophyll profiles in the ocean, and Hardman-Mountford et al. (2003) applied this method to altimeter data. Ultsch and Röske (2002) used it to predict sea level. The SOM technique was also used to extract SST and wind patterns from satellite data (Richardson et al. 2003; Risien et al. 2004), and to detect ocean current spatial patterns from moored velocity time series (Liu and Weisberg 2005b).

b. Growing hierarchical self-organizing map

Despite its wide applications, SOM analysis has inherent deficiencies. First, it uses a static network architecture w.r.t. the number and arrangement of neural nodes that have to be defined prior to the start of training. Second, hierarchical relations between the input data are difficult to detect in the map display. To address both issues within one framework, a neural network model of the growing hierarchical self-organizing map (GHSOM) was recently introduced (Dittenbach et al. 2002; Rauber et al. 2002; Dittenbach 2003; Pampalk et al. 2004). The GHSOM is composed of independent SOMs, each of which is allowed to grow in size during the training process until a quality criterion regarding data representation is met. This growth process is further continued to form a layered architecture such that hierarchical relations between input data are further detailed at lower layers of the neural network. To our knowledge, the GHSOM method has not yet been applied to meteorological or oceanographic research.

c. The SOM and GHSOM MATLAB toolboxes

Most of the above referenced SOM applications in meteorology and oceanography are based on a software package SOM_PAK 3.1 or earlier versions (Kohonen et al. 1995) written in C language. More recently the use of MATLAB, as a high-level programming language with graphics and visualization support, has facilitated an efficient, customizable SOM implementation (Vesanto et al. 2000). The SOM MATLAB Toolbox utilizes MATLAB structures, making it convenient to tailor the code for specific user needs. The SOM Toolbox version 2.0 can be downloaded from a Web site of the Helsinki University of Technology, Finland: http://www.cis.hut.fi/projects/somtoolbox/. The GHSOM Toolbox, developed jointly by the University of Aberdeen and Vienna University of Technology, can be downloaded at http://www.oefai.at/~elias.pampalk/ghsom/.

d. Goal of this paper

A 5-yr set of daily SST composite maps on the WFS is analyzed using the SOM and the GHSOM Toolboxes. The purposes are twofold: 1) to demonstrate the usefulness of the GHSOM in feature extraction, and 2) to describe the characteristic SST patterns on the WFS and their temporal variations.

Since the GHSOM method is new to the meteorological and oceanographic community, a brief discussion on the philosophy behind the SOM and GHSOM techniques is given in section 2. The SST dataset is described in section 3. Applications of linear, EOF, and nonlinear, GHSOM methods are described in sections 4 and 5, respectively. The results are discussed and summarized in section 6.

2. The SOM and GHSOM

This section provides a brief introduction of the SOM and GHSOM methods based on Kohonen (1982, 2001), Dittenbach et al. (2002), Rauber et al. (2002), Dittenbach (2003), and Pampalk et al. (2004). The SOM is a nonlinear, ordered, smooth mapping of high-dimensional input data onto the elements of a regular, low-dimensional (usually 2D) array (Kohonen 1982, 2001). Figure 1 illustrates how the SOM works. The SOM consists of a set of i units arranged in a 2D grid with a weight vector $\mathbf{m}_i$ attached to each unit, which may be initialized randomly. Input vectors $\mathbf{x}$ are presented to the SOM, and the activation of each unit for the presented input vector is calculated using an activation function. Commonly, it is the Euclidian distance between the weight vector of the unit and the input vector that serves as the activation function. In the next step the weight vector of the unit showing the highest activation (i.e., the smallest Euclidian distance) is selected as the "winner" c_k, where

$$c_k = \arg\min\|\mathbf{x}_k - \mathbf{m}_i\|. \quad (1)$$

The weight vector of the winner is moved toward the presented input signal by a certain fraction of the Eu-

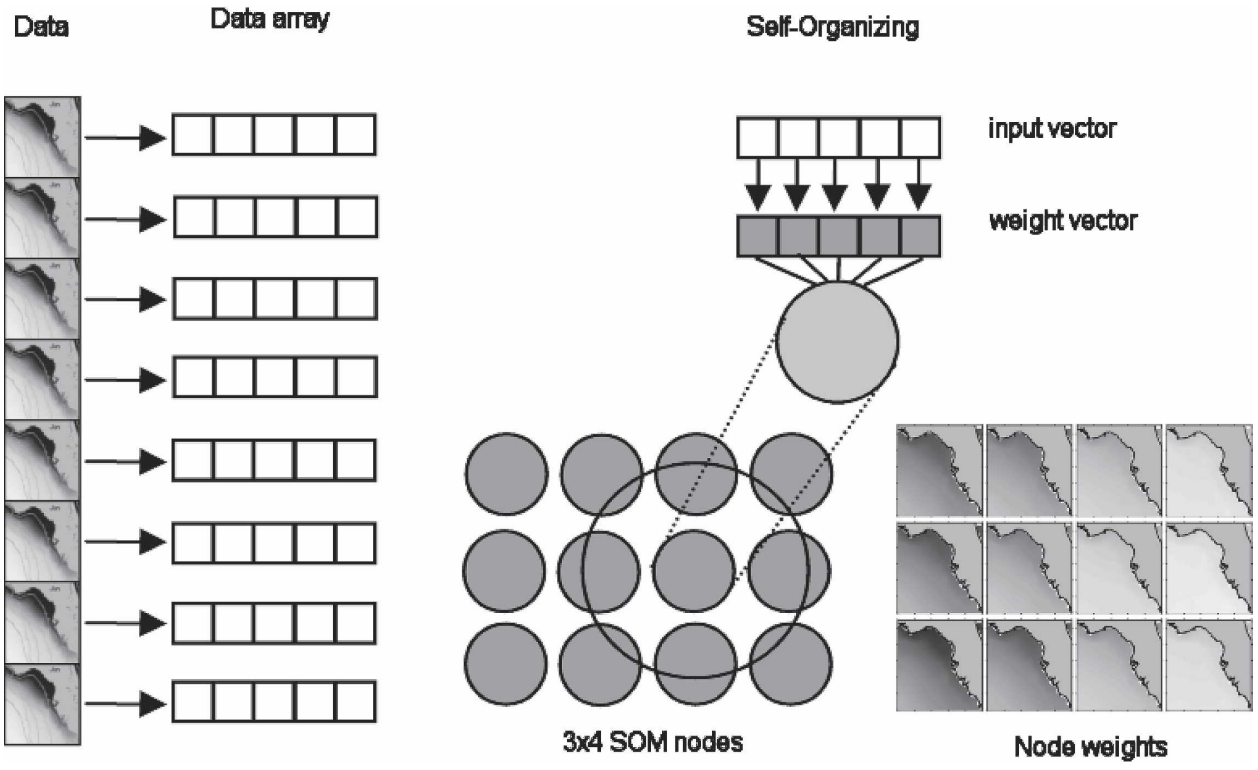

FIG. 1. Illustration of how an SOM works. The data time series are rearranged in a 2D array such that the data at each time step are reshaped as a row vector. For each time step, the row vector is used to update the weight of the SOM via an unsupervised learning algorithm. This iterative process is called self-organizing. The outcome weight vectors of the SOM nodes are reshaped back into characteristic data patterns.

clidean distance as indicated by a time-decreasing learning rate α. The learning rate α can be an inverse time, linear, or power function. Thus, this unit's activation will be even higher the next time the same input signal is presented. Moreover, the weight vectors of units in the neighborhood of the winner are also modified according to a spatial–temporal neighborhood function ε. Similar to the learning rate, the neighborhood function ε is time-decreasing. Also, ε decreases spatially away from the winner. There are many types of neighborhood function, and the typical one is Gaussian. The learning rule may be expressed as

$$\mathbf{m}_i(t+1) = \mathbf{m}_i(t) + \alpha(t) \cdot \varepsilon(t) \cdot [\mathbf{x}(t) - \mathbf{m}_i(t)], \qquad (2)$$

where t denotes the current learning iteration and $\mathbf{x}$ represents the currently presented input pattern. This learning procedure leads to a topologically ordered mapping of the presented input data. Similar patterns are mapped onto neighboring regions on the map, while dissimilar patterns are further apart. One limitation of the SOM is that its size needs to be specified before the training process. The smaller the size, more general information is obtained; the larger the size, more detailed information can be extracted. Additional discussion on the SOM is given in Liu and Weisberg (2005b).

The GHSOM enhances the capabilities of the basic SOM in two ways. The first is to use an incrementally growing version of the SOM, which does not require the user to directly specify the size of the map beforehand; the second enhancement is the ability to adapt to hierarchical structures in the data (Dittenbach et al. 2002; Rauber et al. 2002; Dittenbach 2003; Pampalk et al. 2004). This is illustrated in Fig. 2. Prior to the training process, a "map" in layer 0 consisting of only one unit is created. This unit's weight vector is initialized as the mean of all input vectors and its mean quantization error (MQE) is computed. The MQE of unit i is computed as

$$MQE_i = \frac{1}{|U_i|} \sum_{k \in U_i} \|\mathbf{x}_k - \mathbf{m}_i\|, \qquad U_i = \{k | c_k = i\}. \qquad (3)$$

Beneath the layer 0 map a new SOM is created with a size of initially 2×2 units. The intention is to increase

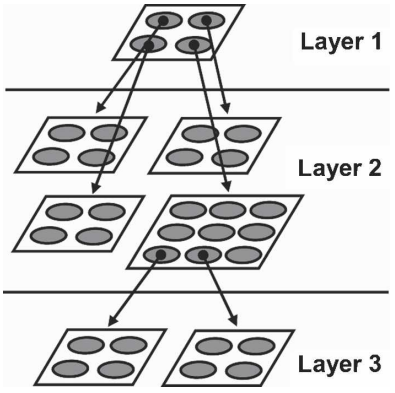

FIG. 2. An example of the hierarchical structure of the GHSOM. All of the four units in the first-layer SOM are expanded in the second layer. Only two units in one of the second-layer SOMs are further expanded in the third layer.

the map size until all data items are represented well. A mean of all MQE_i is obtained as $\langle MQE \rangle$. The $\langle MQE \rangle$ is then compared to the MQE in the layer above, $\langle MQE \rangle_{\text{above}}$. If the following inequality is fulfilled, a new row or column of map units is inserted in the SOM,

$$\langle MQE \rangle > \tau_1 \langle MQE \rangle_{\text{above}}, \tag{4}$$

where τ_1 is a user-defined parameter. Once the decision is made to insert new units, the remaining question is where to do so. In the GHSOM array, the unit i with the largest MQE_i is defined as the error unit. Then the most dissimilar adjacent neighbor, that is, the unit with the largest distance in respect to the model vector, is selected and a new row or column is inserted between these. If the inequality (4) is not satisfied, the next decision to be made is whether some units should be expanded on the next hierarchical level or not. If the data mapped onto one single unit i still has a larger variation, that is,

$$MQE_i > \tau_2 \langle MQE \rangle_{\text{above}}, \tag{5}$$

where τ_2 is a user-defined parameter, then a new map will be added at a subsequent layer. Generally, the values for τ_1 and τ_2 are chosen such that $1 > \tau_1 > > \tau_2 > 0$. In the GHSOM Toolbox, τ_1 and τ_2 are called breadth- and depth-controlling parameters, respectively. Generally, the smaller the parameter τ_1, the larger the SOM arrays will be. The smaller the parameter τ_2, the more layers the GHSOM will have in the hierarchy.

3. Data

A daily composite SST time series was generated for the WFS by merging SST data from the Advanced Very High Resolution Radiometer and the Tropical Rainfall Measuring Mission Microwave Imager using an optimal interpolation scheme (He et al. 2003). We chose the initial 5-yr period spanning January 1998 through December 2002 for an analysis here. The data domain is shown in Fig. 3, which is a little smaller than that of He et al. (2003), focusing more on the WFS. If the dataset is arranged in an $I \times J$ matrix, where I and J are spatial and temporal dimensions, respectively, then a temporal mean SST pattern is expressed as

$$\overline{T}(x) = \frac{1}{J} \sum_{j=1}^{J} T(x, t_j), \tag{6}$$

and shown in Fig. 3. The 5-yr mean pattern shows the warm Loop Current water seaward of the shelf break and the relatively cooler water along the coast near the Florida Big Bend region. The SST gradient points from the southwest to the northeast, with an approximate 30°~40° angle deviation from the mean along-isobath direction. This may reflect the combined effects of latitudinal differences in surface heating due to solar radiation and across-shelf differences in water column heating/cooling due to the depth gradient on the shelf.

Two types of SST anomalies are prepared. The first type, $\hat{T}(x, t)$, is obtained by subtracting the temporal mean map from the original data

$$\hat{T}(x, t) = T(x, t) - \overline{T}(x). \tag{7}$$

By further subtracting a time series of spatial mean values, which is expressed as

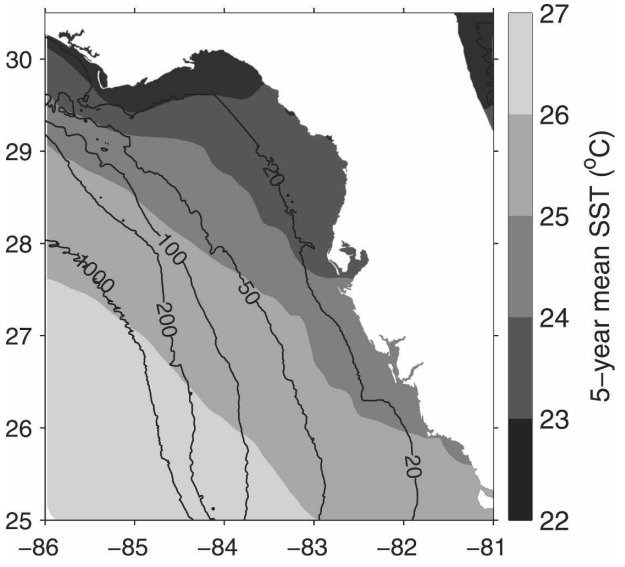

FIG. 3. A record-length mean SST map for the 5-yr period, 1998–2002, overlaid on the 20-, 50-, 100-, 200-, and 1000-m isobaths for the WFS analysis domain.

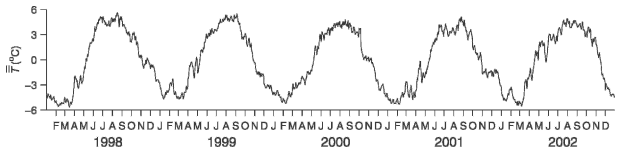

FIG. 4. Time series of the spatial mean SST anomaly for this WFS analysis domain.

$$\overline{\overline{T}}(t) = \frac{1}{I}\sum_{i=1}^{I} \hat{T}(x_i, t), \tag{8}$$

a second type SST anomaly, $\tilde{T}(x, t)$, is obtained as

$$\tilde{T}(x, t) = T(x, t) - \overline{T}(x) - \overline{\overline{T}}(t). \tag{9}$$

The spatial mean SST anomaly has higher values in summer and lower values in winter, and the temporal variation is similar to a sine function (Fig. 4).

The monthly mean SST patterns, computed over the entire 5-yr analysis period, show a seasonal variation (Fig. 5). An across-shelf SST gradient is found in all the winter months, but it is not obvious in the summer months. A spring cold tongue structure that is prominent in April and May is consistent with previous literature (e.g., Weisberg et al. 1996; He and Weisberg 2002). These SST features will be used for comparison with those derived from linear EOF and nonlinear GHSOM analyses.

4. EOF patterns of the SST

Before performing the SOM and GHSOM analyses, we begin with the more established technique of time

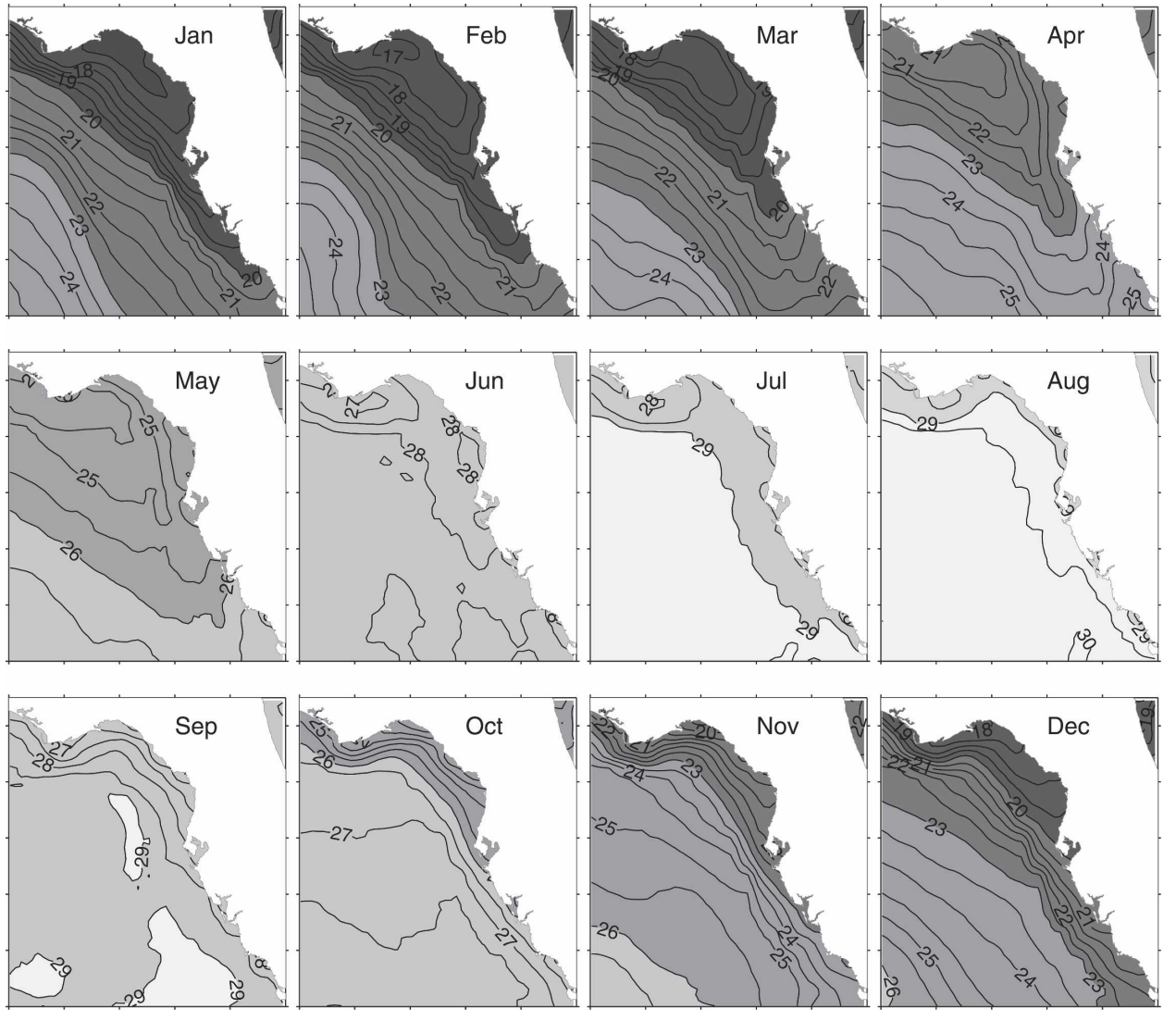

FIG. 5. SST monthly means on the WFS obtained by forming an average for each month over the 5-yr period 1998–2002.

domain EOF that has wide oceanographic and meteorological applications (e.g., Weare et al. 1976; Richman 1986; Lagerloef and Bernstein 1988; Chu et al. 1997a,b; He et al. 2003; Espinosa-Carreon et al. 2004). The EOF is the same as the principal component (PC) analysis (Hotelling 1933) used in the statistics community. In the combined parlance the PCs are the amplitudes, which are functions of time, of their corresponding spatial eigenfunctions, or EOFs, and the analysis separates the datasets into orthogonal modes. Generally speaking, each mode n has an associated variance, a dimensional spatial pattern $F_n(x)$, and a nondimensional time series $\alpha_n(t)$. Thus, the SST anomalies $\hat{T}(x, t)$ may be represented by the EOFs as

$$\hat{T}(x, t) = \sum_{n=1}^{N} \alpha_n(t) F_n(x). \tag{10}$$

He et al. (2003) reported EOF results for the first type of SST anomaly defined previously. The first three EOFs of that analysis account for 90.6%, 3.5%, and 0.9% of the SST variance, respectively. The dominant first mode represents the seasonal surface heat flux cycle. Note that the strong seasonal variation may hinder our view of other interesting processes. To reduce the impact of the seasonal cycle on the data analysis, the second type of SST anomaly data $\tilde{T}(x, t)$ are used, wherein both the temporal mean map and the spatial mean SST time series are removed from the original SST. Some previous studies removed the seasonal cycle by fitting each time series to annual and semiannual harmonics and subtracting them from the original data (Espinosa-Carreon et al. 2004). In that way, the amplitude of the harmonics being removed may be different from one point to another on a map. We choose to subtract a time series of spatial mean SST simply because the main purpose of the study is to extract the spatial patterns and it is better not to change the relative values on an SST map. Our EOF results are shown in Fig. 6. The first mode, although accounting for a smaller percentage of SST variance (59.6%), has a spatial pattern and temporal variation essentially the same as those in He et al. (2003). It represents the seasonal surface heat flux cycle; that is, the PC time series has an annual periodicity peaking in summer and winter, and the eigenfunction shows two different regimes: the wide WFS and the deep ocean. This is a consequence of water depth and the buffering effect on the temperature by the warm water advection of the Loop Current. Thus, the Loop Current presents the WFS with a cooling tendency in summer and a warming tendency in winter. The second mode, accounting for 10.8% of the SST variance, reveals a warm/cold tongue pattern on the WFS. The spring cold tongue on the mid-WFS is due to the combined baroclinic and barotropic responses of the WFS circulation to the seasonal surface heat and momentum fluxes as described in previous studies (Weisberg et al. 1996; He and Weisberg 2002; He et al. 2003). The third mode, accounting for 6.4% of the SST variance, reveals a pattern of the shelf break Loop Current eddy. The fourth (and higher) mode revealing smaller spatial structures and higher frequency PC fluctuations are beginning to describe the synoptic-scale variability.

5. GHSOM mapping of the SST

In this section, the GHSOM is performed on the original SST data and the SST anomaly data, $\hat{T}(x, t)$ and $\tilde{T}(x, t)$, respectively.

a. GHSOM analysis of the original SST data

The 5-year-long daily SST data are used as input to the GHSOM without any preconditioning. In the application of the GHSOM Toolbox, all the parameters are set to the default values except τ_1 and τ_2, the breadth- and depth-controlling parameters. Different (τ_1, τ_2) values are used to test the GHSOM performance (see Table 1). Generally, when smaller (τ_1, τ_2) values are chosen there are more nodes, that is, larger SOM arrays, in the output. A large SOM array identifies a large number of patterns and reveals more detailed structure within the data, whereas a small SOM array identifies fewer, more generalized patterns. We chose the case of $(\tau_1 = 0.6, \tau_2 = 0.06)$ to analyze simply because the results have two layers and the SOM arrays are large enough to represent characteristic SST features and small enough to be visualized.

The layer-1 GHSOM enables a nonlinear classification of the 5-year-long daily SST on the WFS into four categories, as shown in the 2×2 SOM array in Fig. 7. Each unit explains a particular set of SST characteristics. Unit 1 reveals a typical low SST pattern ($16°C < SST < 25°C$) in which the isotherms are approximately aligned with the isobaths, with the coldest water centered around Florida Big Bend region and with the warmest water seaward of the shelf break associated with the Loop Current. Unit 4 reveals a high SST pattern ($SST > 28°C$), with no obvious horizontal temperature gradient. Both units 2 and 3 are transitional patterns between the units 1 and 4 extremes.

For each of the 5-year-long daily SST maps, a best-matching unit (BMU) can be identified. The BMU is defined to have the smallest weighted distance from the input data. Time series of the BMU (given by its num-

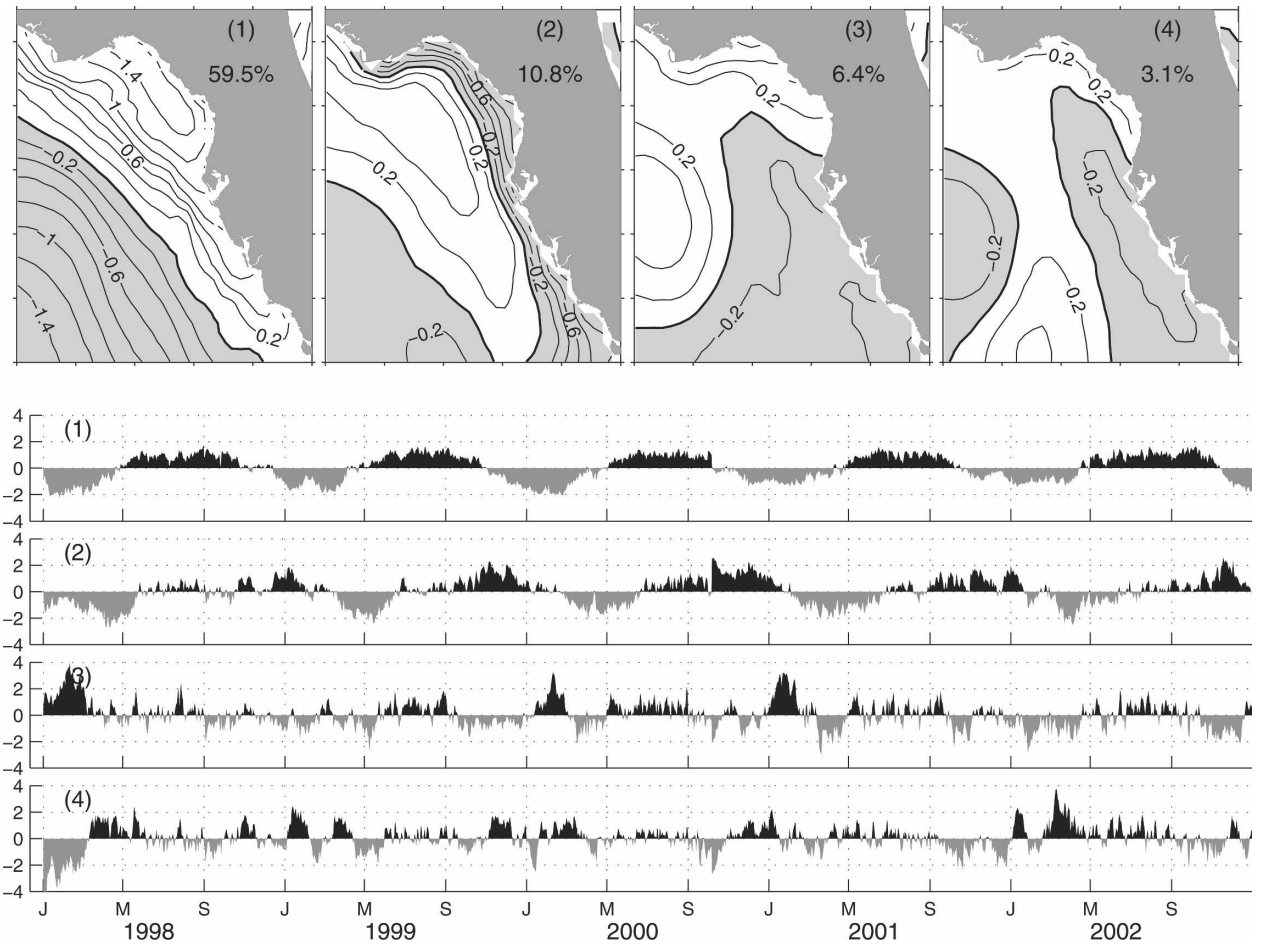

FIG. 6. Eigenfunctions and the associated temporal evolution functions for the first four EOF modes of the SST data. The percent of variance accounted for by each mode is indicated at the upper-right corner of each eigenfunction plot. The labels J, M, and S on the abscissa designate the first days of January, May, and September, respectively, here and in subsequent figures.

ber, 1–4) show obvious seasonal fluctuations (Fig. 8). Unit 1 is best matched in winter, while unit 4 is best matched in summer. Unit 2 is best matched in spring and early winter, and unit 3 in early summer and autumn. The cycle of units $1 \rightarrow 2 \rightarrow 3 \rightarrow 4 \rightarrow 3 \rightarrow 2 \rightarrow 1$ therefore takes place in a year. To quantify the representation of each unit (1–4), the frequency of occurrence is computed by summing the hits of that unit and dividing by the total record length. The relative frequency of occurrence of each unit is shown in the upper-right corner of each map in Fig. 7. For example, units 1 and 4 represent 26.3% and 33.7% of all the SST data, respectively. A monthly climatology of the frequency of occurrence during the 5 years (Fig. 9) shows that the first pattern appears mostly in January–March, the second in April, November, and December, the third in May and October, and the fourth in June–September.

TABLE 1. Total numbers of the SOM units in the GHSOM with different values of controlling parameters. It is the third case (shown in bold type) that is presented in this paper.

τ_1	τ_2	Layer 1 SOM	Layer 2 SOM
0.8	0.08	4	4, 0, 0, 4
0.7	0.07	4	6, 4, 0, 4
0.6	**0.06**	**4**	**12, 6, 0, 10**
0.5	0.05	4	30, 15, 18, 55
0.4	0.04	4	64, 40, 48, 119
0.3	0.03	6	132, 120, 96, 0, 144, 140
0.2	0.02	24	0
0.1	0.01	95	0

Not all units in the first layer grow to the same depth in the GHSOM hierarchy. Only units 1, 2, and 4 are further expanded in a second-layer map. The second-layer GHSOM grown from unit 1 (winter SST patterns) of the first-layer GHSOM (GHSOM 2–1) is shown in Fig. 10. Different features of the cold coastal water and the warm Loop Current water are classified into the 3

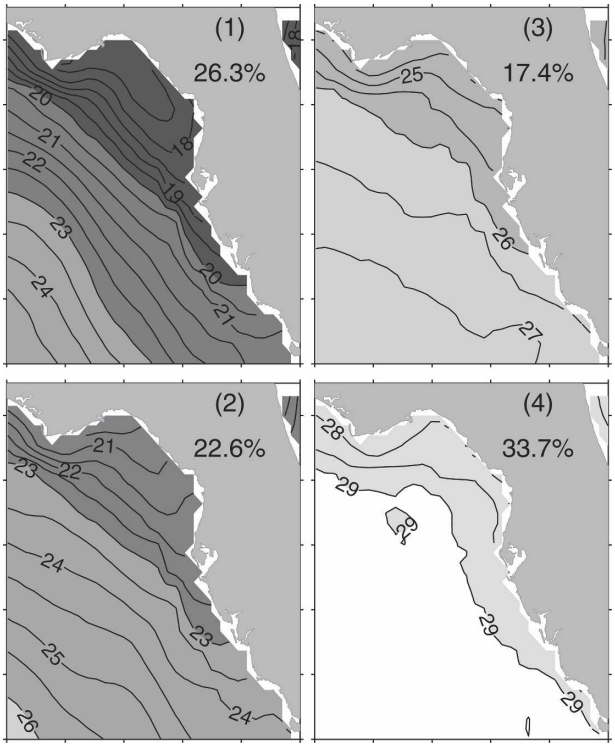

FIG. 7. Layer 1 GHSOM (2 × 2) for the 5-yr-long daily SST data on the WFS. The frequency of occurrence of each pattern is also shown on each map.

× 4 SOM array. Unit 2 of this 3 × 4 s layer has the highest frequency of occurrence (12.9%), showing a typical Loop Current feature seaward of the shelf break. Note that the relative frequency of occurrence here is referred to the total number of hits of unit 1 in the first layer only; that is, the frequency of occurrences for each of the sublayer SOMs sum to 100%. The second-layer GHSOM grown from unit 2 (spring and early winter SST patterns) of the first-layer GHSOM (GHSOM 2–2) is shown in Fig. 11. Specifically, the upper three units (1, 3, and 5) represent spring patterns, while the lower units (2, 4, and 6) represent early winter patterns, and this is evident in the time series of the BMUs (Fig. 12). The general sequence of the SST variation is units 1 → 3 → 5 for the spring evolution and units 6 → 4 → 2 for the early winter evolution. The spring cold tongue structure may be identified in units 3 and 5.

The second layer GHSOM grown from unit 4 (summer SST patterns) of the first-layer GHSOM (GHSOM 2–4, a 2 × 5 array) is shown in Fig. 13. The peak summer SST patterns are shown in the rhs of the SOM array (units 7~10), while the early and late summer SST patterns are arranged in the lhs (units 1~6). The evolution of the summer SST patterns from early to late summer stages in each year is illustrated in Fig. 14. The general characteristic of summer SST is uniformly high temperature. Thus, it is difficult to divide the coastal and the Loop Current waters based on summer SST.

b. *GHSOM analysis of the SST anomaly with the temporal mean map removed*

Here the SST anomaly $\hat{T}(x, t)$ is used as input to the GHSOM analysis. Similar to that in section 5a, a set of controlling parameters are used to run the GHSOM model, and when $\tau_1 = 0.2$ and $\tau_2 = 0.02$ the GHSOM has only one layer (24 units). This case is chosen to demonstrate the capability of the GHSOM to function as a basic SOM. A 4 × 6 SOM array of 5-year-long daily SST anomalies is shown in Fig. 15. Similar SST patterns are located adjacent to one another in the SOM mapping, while dissimilar patterns are at the opposite extremes of the SOM space. There is a continuum of change across the SOM array, with the typical summer and winter SST anomaly patterns at the lower-right and upper-left hand corners, respectively, and an annual cycle is obvious in the BMU time series (Fig. 16). For either peak winter (January ~ February) or peak summer (July ~ August) patterns, the SST anomaly is smaller on the ocean side and larger on the shelf with the largest SST anomaly near the coast of the Florida Big Bend. This result is the same as that from the first

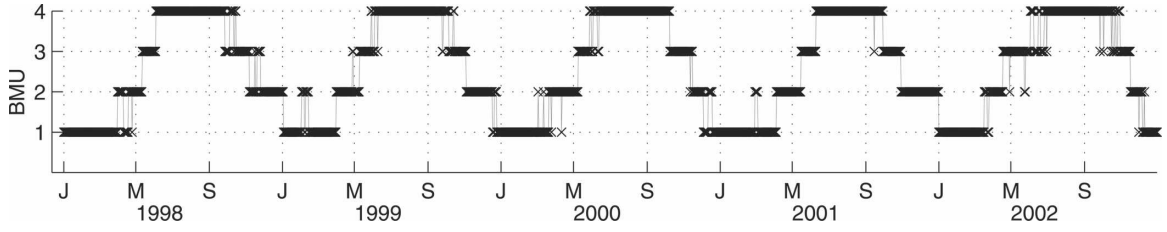

FIG. 8. Temporal evolution of the BMUs (labeled 1–4 on the ordinate) corresponding to the patterns in the layer 1 GHSOM of Fig. 7.

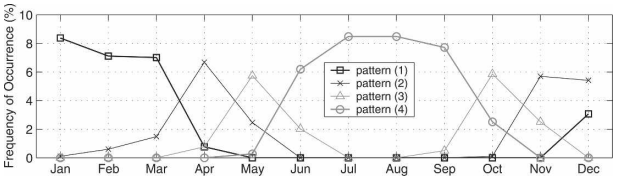

FIG. 9. Frequency of occurrence of the layer 1 GHSOM (Fig. 7) patterns as a function of month.

EOF mode (Fig. 6). The spring cold tongue structure may be identified only in unit 5, while the warm tongue structure may be identified in many units (10, 14, and 16).

c. *GHSOM analysis of the SST anomaly with both the temporal mean map and spatial mean time series removed*

Here the SST anomaly $\tilde{T}(x, t)$ is used in the GHSOM model. By removing the time series of spatial mean SST, the strong seasonal variation is reduced, while the relative spatial structure is not altered; that is, the horizontal SST gradient is not changed. Similar to that in section 5a, a set of controlling parameters are used to run the GHSOM model. We present the results of $\tau_1 = 0.8$ and $\tau_2 = 0.08$ for the same reason as in section 5a.

The first layer GHSOM is still a 2×2 array repre-

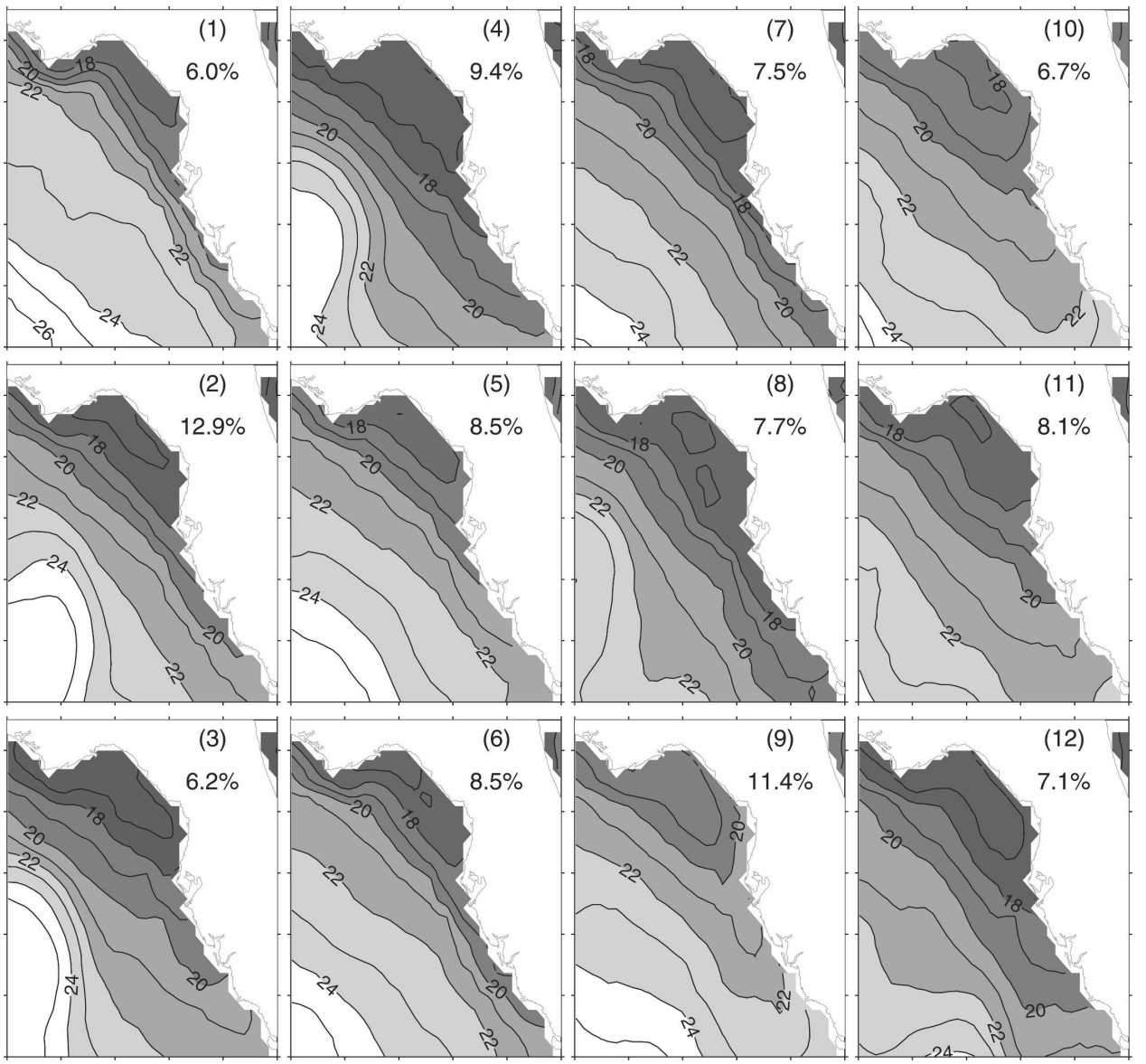

FIG. 10. GHSOM 2–1: The layer 2 SOM expanded from pattern 1 of the first-layer GHSOM. The relative frequency of occurrence of each pattern is shown in the upper-right corner of each map.

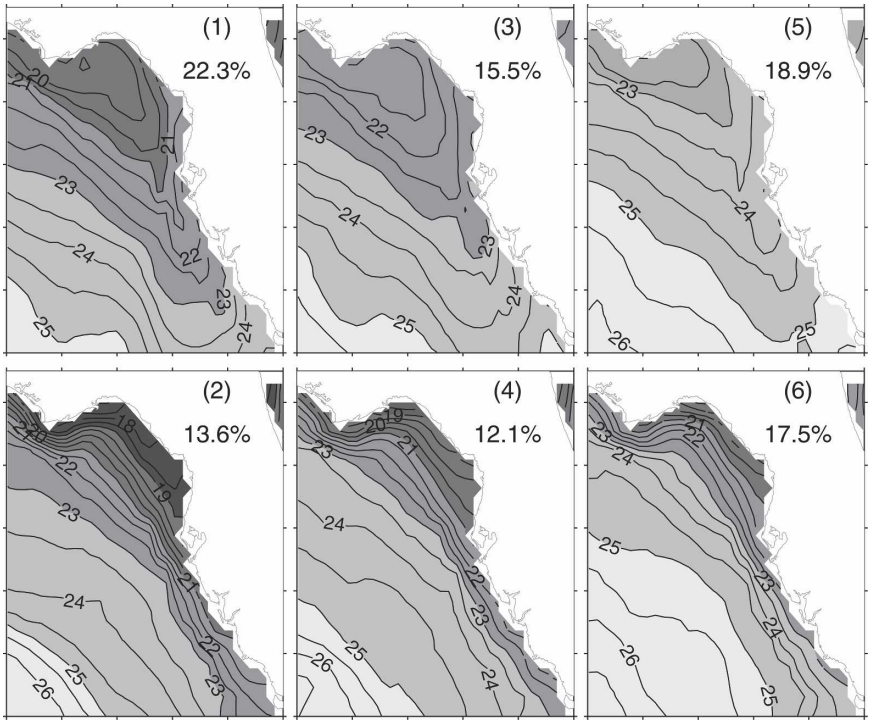

FIG. 11. GHSOM 2–2: The layer 2 SOM expanded from pattern 2 of the first-layer GHSOM. The relative frequency of occurrence of each pattern is shown in the upper-right corner of each map.

senting four categories of the SST anomaly patterns on the WFS (Fig. 17). Unit 1 reveals a wide warm tongue structure on the shelf, mostly appearing in November as a fall transition (Fig. 18); in contrast, unit 4 reveals a spring cold tongue structure on the shelf (peaking in April). Unit 2 reveals a pattern with a coastal and deep ocean contrast in summer (from June to September). On the other hand, unit 3 shows the reverse of the unit 2 pattern in winter (from January to February). Units 1~4 represent 16.3%, 43.6%, 24.4%, and 15.7% of the SST anomaly maps, respectively. Generally, the SST anomaly patterns revealed by the GHSOM may be compared with the first two mode EOFs. Units 2 and 3 resemble the two extremes of the first mode eigenvector with positive and negative weights, respectively; and units 1 and 4 may be ascribed to the second mode EOF with negative and positive weights, respectively. However, the amplitudes of the winter SST anomalies (unit 3) are larger than those of the summer SST anomalies (unit 2). Also, the shapes of the cold and warm tongues are different as shown in units 4 and 1, respectively. These asymmetric phenomena are not identified in the lowest mode EOF results. We note that all the four units may be further expanded in a subsequent layer to reveal more detailed structures, but these are not pursued here.

6. Discussion and summary

As a data analysis method, the EOF conveniently orders patterns of variability on the basis of variance.

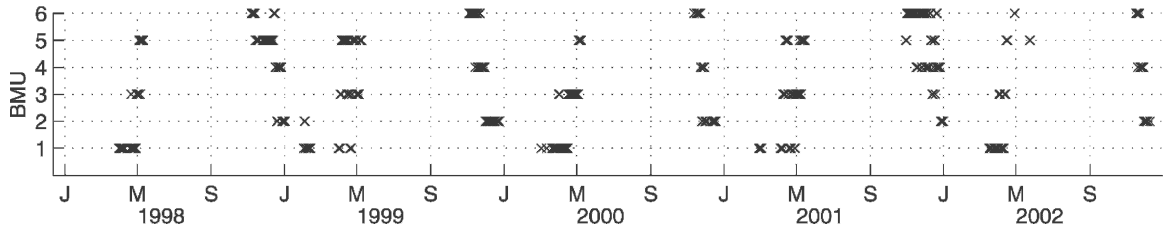

FIG. 12. Temporal evolution of the BMUs for the GHSOM 2–2.

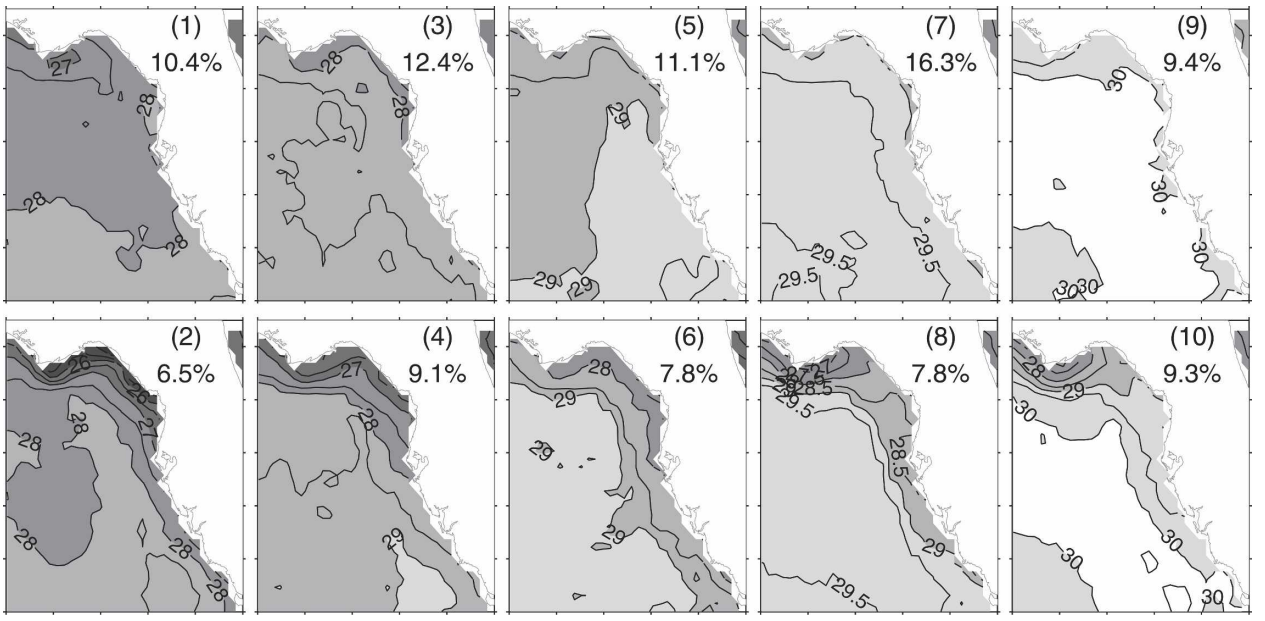

FIG. 13. GHSOM 2–4: The layer 2 SOM expanded from pattern 4 of the first-layer GHSOM. The relative frequency of occurrence of each pattern is shown in the upper-right corner of each map.

However, as a linear method, it may be a suboptimal way of spanning a data space if the system is nonlinear. The nonlinear SOM orders patterns of variability on the basis of topology rather than the variance. A major strength of the SOM is that the underlying patterns in a dataset can be visualized in the same form as the original data. Thus, if input data are SST images, then the outputs are SST patterns, not SST anomaly patterns. This is an advantage over the EOF, in which the temporal mean field is removed prior to the analysis. As the SOM output patterns resemble the input format, their qualitative interpretation may be easier than that from the EOF. Also, the SOM is not subject to the symmetry bias of a given EOF mode, such that the SOM patterns may be more realistic than the EOF patterns. As shown in section 5c, the asymmetric SST anomaly patterns of winter and summer and of the cold and warm tongues revealed by the SOM cannot be identified in the individual EOF patterns. Another advantage of the SOM analysis is that the algorithm is robust in handling missing data, without a priori estimation. Thus, the SOM method can be used to explore incomplete datasets. Moreover, the SOM can be used as a data interpolation technique, estimating missing data from input data that are similar (Hewitson and Crane 2002).

The major advantages of the GHSOM model over the standard SOM are the following. First, the overall training time is reduced since only a necessary number of units are developed to organize the data at a certain level of detail. Second, the GHSOM uncovers the hierarchical structure of the data, allowing the user to understand and analyze a large amount of data in an exploratory way. Each SOM array in the hierarchy explains a particular set of characteristics of the data. This makes the GHSOM analysis an excellent tool for feature extraction and classification. Third, the size of the SOM array does not have to be specified subjectively

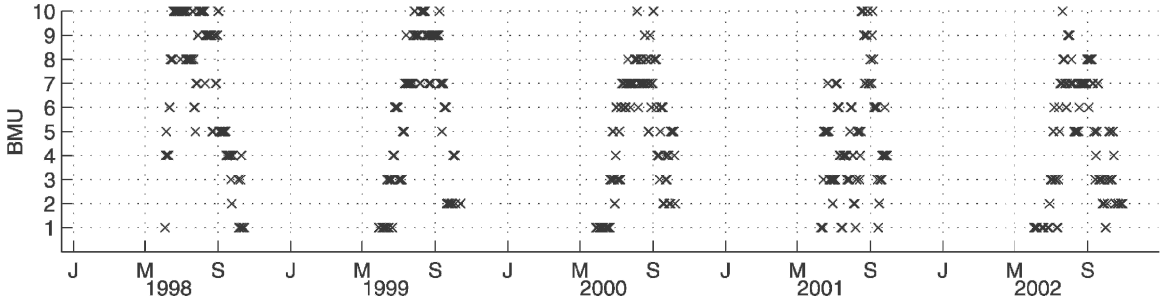

FIG. 14. Temporal evolution of the BMUs for the GHSOM 2–4.

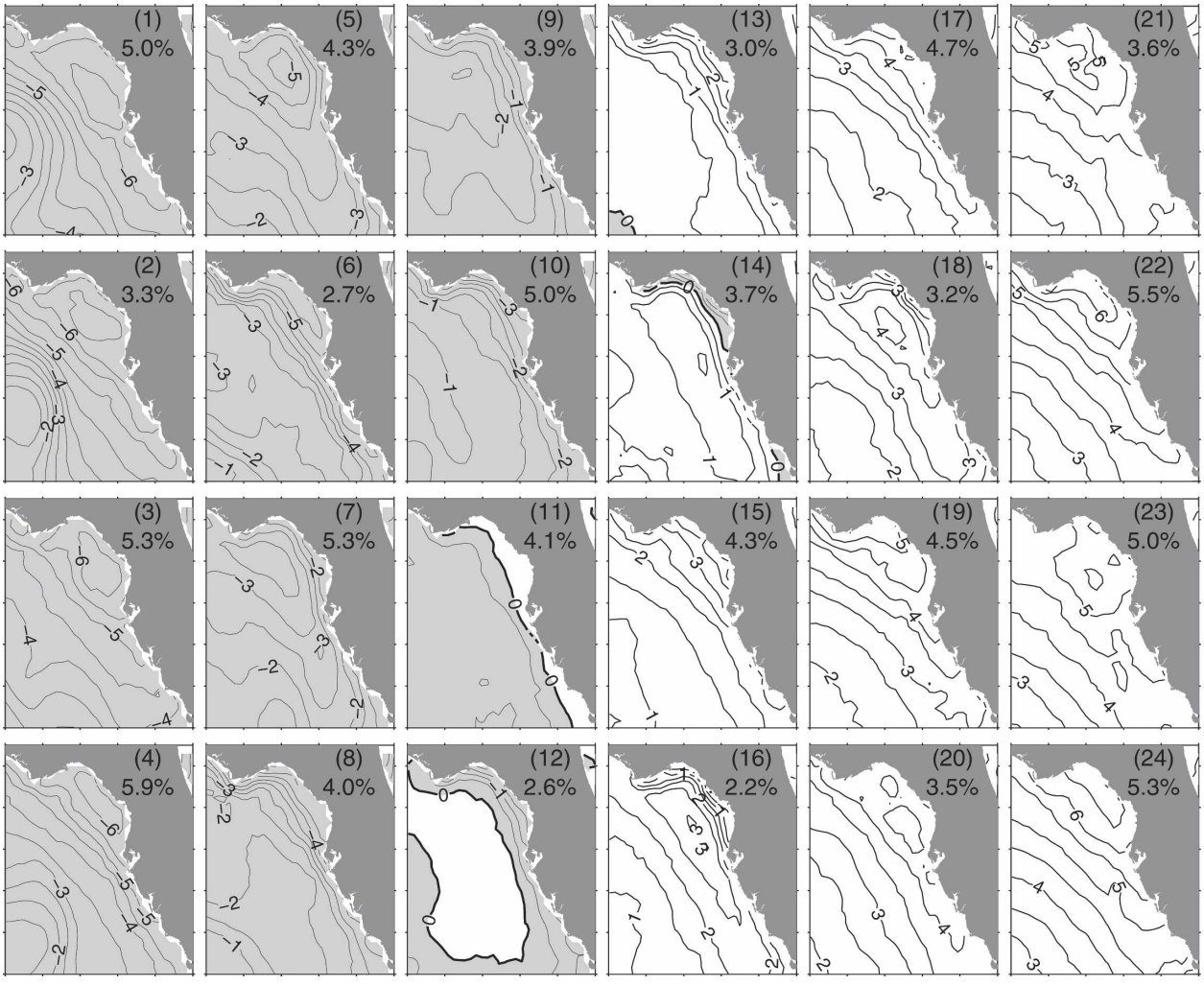

FIG. 15. A 4 × 6 SOM of the 5-yr-long daily SST anomalies. The data are preprocessed by removing the temporal mean map (Fig. 3). The relative frequency of occurrence of each pattern is shown in the upper-right corner of each map.

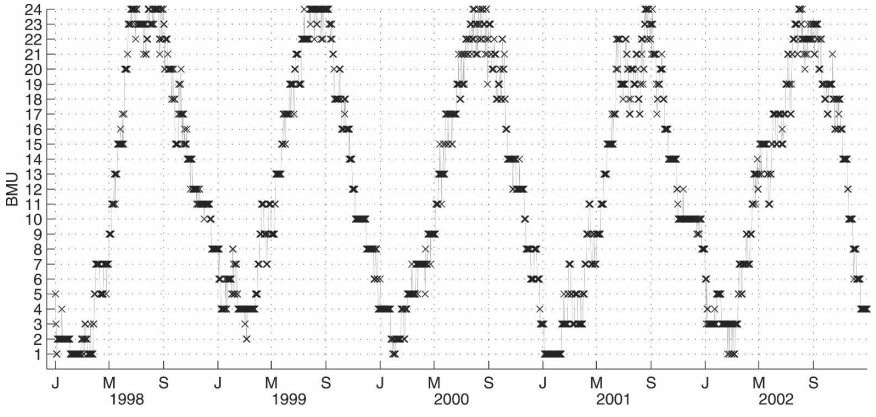

FIG. 16. Temporal evolution of the BMUs for the 4 × 6 SOM in Fig. 15.

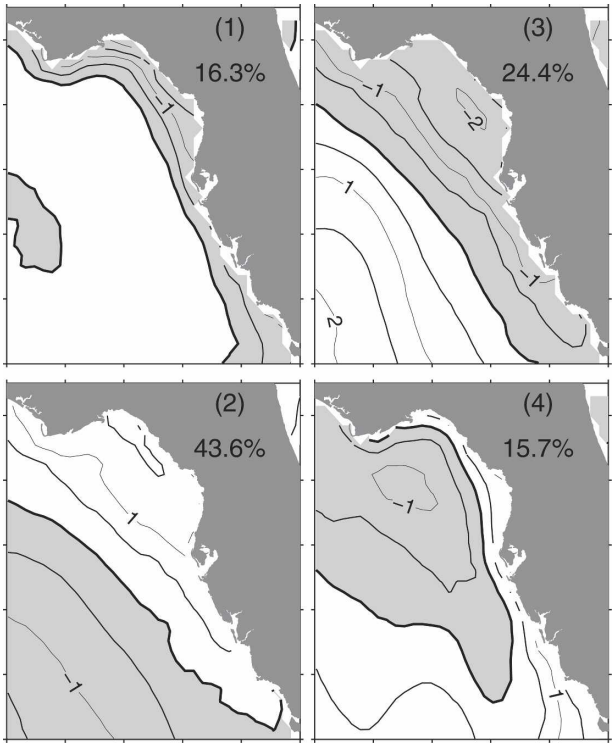

FIG. 17. The layer 1 GHSOM (2 × 2) of the 5-yr-long daily SST anomalies ($\tau_1 = 0.8$, $\tau_2 = 0.08$). The input data are preprocessed by removing both the temporal mean map and a time series of spatial mean values. The relative frequency of occurrence of each pattern is shown in the upper-right corner of each map.

before hand; the GHSOM automatically expands in a three-dimensional structure.

Here we used the GHSOM method to extract characteristic patterns of SST variability on the WFS from a time series of daily SST maps that span the 5-year interval 1998~2002. Four characteristic SST patterns are extracted in the first-layer GHSOM array: characteristic winter and summer patterns, and two transitional patterns. Three of these are further expanded in a second layer, yielding more pattern evolution details. The results show that a seasonal cycle dominates the SST variability on the shelf. Winter SST is characterized by cold water (16°C < SST < 25°C) with the isotherms aligned approximately along the isobaths and with the coldest water centered within the Florida Big Bend region and with the warmest water located seaward of shelf break in association with the Loop Current. In contrast, summer SST is characterized by horizontally uniform, warm water (SST > 28°C) making it difficult to discern shelf from Loop Current waters. The spring transition includes a midshelf cold tongue.

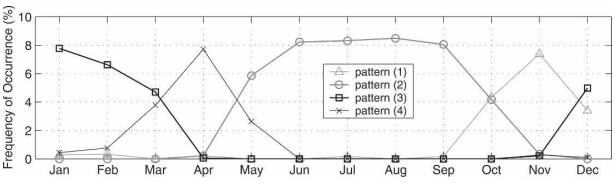

FIG. 18. Frequency of occurrence of the four characteristic maps in Fig. 17 as a function of month.

When the GHSOM analysis is performed on the SST anomaly data (with both the temporal mean map and the time series of spatial mean values removed), four characteristic SST anomaly patterns are also obtained in the first GHSOM layer, representing the SST anomaly patterns in the four seasons. The winter SST anomaly pattern shows the cooling effect of shoaling isobaths on shelf and the warming influence of advection by the Loop Current, while the summer pattern reveals the warming effect of shoaling isobaths on shelf relative to the Loop Current. The spring pattern shows a midshelf cold tongue, while the fall pattern shows a warm tongue on the shelf. These seasonal patterns, whether extracted from the original data or the anomaly fields, exhibit asymmetries that are not readily apparent in the complementary EOF analysis.

Acknowledgments. Support was provided by the Office of Naval Research under Grant N00014-98-1-0158 for observations and modeling of the west Florida continental shelf circulation and Grant N00014-02-1-0972 for the Southeast Atlantic Coastal Ocean Observing System.

REFERENCES

Ainsworth, E. J., 1999: Visualization of ocean colour and temperature from multispectral imagery captured by the Japanese ADEOS satellite. *J. Visual.,* **2,** 195–204.

——, and S. F. Jones, 1999: Radiance spectra classification from the ocean color and temperature scanner on ADEOS. *IEEE Trans. Geosci. Remote Sens.,* **37,** 1645–1656.

Ambroise, C., G. Seze, F. Badran, and S. Thiria, 2000: Hierarchical clustering of self-organizing maps for cloud classification. *Neurocomputing,* **30,** 47–52.

Cavazos, T., 1999: Large-scale circulation anomalies conducive to extreme events and simulation of daily rainfall in northeastern Mexico and southeastern Texas. *J. Climate,* **12,** 1506–1523.

——, 2000: Using self-organizing maps to investigate extreme climate events: An application to wintertime precipitation in the Balkans. *J. Climate,* **13,** 1718–1732.

——, A. C. Comrie, and D. M. Liverman, 2002: Intraseasonal variability associated with wet monsoons in southeast Arizona. *J. Climate,* **15,** 2477–2490.

Chu, P. C., S. H. Lu, and Y. Chen, 1997a: Temporal and spatial variabilities of the South China Sea surface temperature anomaly. *J. Geophys. Res.,* **102,** 20 937–20 955.

——, H. C. Tseng, C. P. Chang, and J. M. Chen, 1997b: South China Sea warm pool detected from the Navy's Master Oceanographic Observational Data Set (MOODS). *J. Geophys. Res.,* **102**, 15 761–15 771.

Dittenbach, M., 2003: The growing hierarchical self-organizing map: Uncovering hierarchical structure in data. *J. Austrian Soc. Artif. Intell.,* **22** (3), 25–28.

——, A. Rauber, and D. Merkl, 2002: Uncovering the hierarchical structure in data using the Growing Hierarchical Self-Organizing Map. *Neurocomputing,* **48,** 199–216.

Espinosa-Carreon, T. L., P. T. Strub, E. Beier, F. Ocampo-Torres, and G. Gaxiola-Castro, 2004: Seasonal and interannual variability of satellite-derived chlorophyll pigment, surface height, and temperature off Baja California. *J. Geophys. Res.,* **109,** C03039, doi:10.1029/2003JC002105.

Gilbes, F., C. Tomas, J. J. Walsh, and F. E. Muller-Karger, 1996: An episodic chlorophyll plume on the West Florida Shelf. *Cont. Shelf Res.,* **16,** 1201–1224.

Hardman-Mountford, N. J., A. J. Richardson, D. C. Boyer, A. Kreiner, and H. J. Boyer, 2003: Relating sardine recruitment in the Northern Benguela to satellite-derived sea surface height using a neural network pattern recognition approach. *Progress in Oceanography,* Vol. 59, Pergamon, 241–255.

He, R., and R. H. Weisberg, 2002: West Florida shelf circulation and temperature budget for the 1999 spring transition. *Cont. Shelf Res.,* **22,** 719–748.

——, and ——, 2003: West Florida shelf circulation and temperature budget for the 1998 fall transition. *Cont. Shelf Res.,* **23,** 777–800.

——, ——, H. Zhang, F. Muller-Karger, and R. W. Helber, 2003: A cloud-free, satellite-derived, sea surface temperature analysis for the West Florida Shelf. *Geophys. Res. Lett.,* **30,** 1811, doi:10.1029/2003GL017673.

Hewitson, B. C., and R. G. Crane, 1994: *Neural Nets: Applications in Geography*. Kluwer Academic, 208 pp.

——, and ——, 2002: Self-organizing maps: Applications to synoptic climatology. *Climate Res.,* **22,** 13–26.

Hong, Y., K. Hsu, S. Sorooshian, and X. Gao, 2004: Precipitation estimation from remotely sensed imagery using an artificial neural network cloud classification system. *J. Appl. Meteor.,* **43,** 1834–1853.

Hotelling, H., 1933: Analysis of a complex of statistical variables into principal components. *J. Educ. Psych.,* **24,** 417–441.

Hsu, K., H. V. Gupta, X. Gao, S. Sorooshian, and B. Imam, 2002: SOLO—An artificial neural network suitable for hydrologic modeling and analysis. *Water Resour. Res.,* **38,** 1302, doi:10.1029/2001WR000795.

Huh, O. K., W. J. Wiseman, and L. J. Rouse, 1981: Intrusion of loop current waters onto the West Florida continental shelf. *J. Geophys. Res.,* **86,** 4186–4192.

Kaski, S., J. Kangas, and T. Kohonen, 1998: Bibliography of Self-Organizing Map (SOM) papers: 1981–1997. *Neural Comput. Surv.,* **1,** 102–350.

Kohonen, T., 1982: Self-organized information of topologically correct features maps. *Biol. Cybernetics,* **43,** 59–69.

——, 2001: *Self-Organizing Maps*. Springer Series in Information Sciences, Vol. 30, 3d ed., Springer-Verlag, 501 pp.

——, J. Hynninen, J. Kangas, and J. Laaksonen, 1995: SOM_PAK, the self-organizing map program, version 3.1. Helsinki University of Technology, Laboratory of Computer and Information Science, Finland, 27 pp. [Available online at http://www.cis.hut.fi/research/som_pak/.]

Lagerloef, G. S. E., and R. L. Bernstein, 1988: Empirical orthogonal function analysis of Advanced Very High Resolution Radiometer surface temperature patterns in Santa Barbara Channel. *J. Geophys. Res.,* **93,** 6863–6873.

Liu, Y., and R. H. Weisberg, 2005a: Momentum balance diagnoses for the West Florida Shelf. *Cont. Shelf Res.,* **25,** 2054–2074.

——, and ——, 2005b: Patterns of ocean current variability on the West Florida Shelf using the self-organizing map. *J. Geophys. Res.,* **110,** C06003, doi:10.1029/2004JC002786.

Malmgren, B. A., and A. Winter, 1999: Climate zonation in Puerto Rico based on principal components analysis and an artificial neural network. *J. Climate,* **12,** 977–985.

Molinari, R. L., S. Baig, D. W. Behringer, G. A. Maul, and R. Legeckis, 1977: Winter intrusions of the loop current. *Science,* **198,** 505–506.

Oja, M., S. Kaski, and T. Kohonen, 2003: Bibliography of Self-Organizing Map (SOM) papers: 1998–2001 addendum. *Neural Comput. Surv.,* **3,** 1–156.

Paluszkiewicz, T., L. P. Atkinson, E. S. Posmentier, and C. R. McClain, 1983: Observations of a loop current frontal eddy intrusion onto the West Florida Shelf. *J. Geophys. Res.,* **88C,** 9639–9651.

Pampalk, E., G. Widmer, and A. Chan, 2004: A new approach to hierarchical clustering and structuring of data with Self-Organizing Maps. *Intell. Data Anal. J.,* **8** (2), 131–149.

Rauber, A., D. Merkl, and M. Dittenbach, 2002: The Growing Hierarchical Self-Organizing Map: Exploratory analysis of high-dimensional data. *IEEE Trans. Neural Networks,* **13,** 1331–1341.

Richardson, A. J., M. C. Pfaff, J. G. Field, N. F. Silulwane, and F. A. Shillington, 2002: Identifying characteristic chlorophyll a profiles in the coastal domain using an artificial neural network. *J. Plankton Res.,* **24,** 1289–1303.

——, C. Risien, and F. A. Shillington, 2003: Using self-organizing maps to identify patterns in satellite imagery. *Progress in Oceanography,* Vol. 59, Pergamon, 223–239.

Richman, M. B., 1986: Rotation of principal components. *J. Climatol.,* **6,** 293–335.

Risien, C. M., C. J. C. Reason, F. A. Shillington, and D. B. Chelton, 2004: Variability in satellite winds over the Benguela upwelling system during 1999–2000. *J. Geophys. Res.,* **109C,** C03010, doi:10.1029/2003JC001880.

Silulwane, N. F., A. J. Richardson, F. A. Shillington, and B. A. Mitchell-Innes, 2001: Identification and classification of vertical chlorophyll patterns in the Benguela upwelling system and Angola-Benguela Front using an artificial neural network. *S. Afr. J. Mar. Sci.,* **23,** 37–51.

Ultsch, A., and F. Röske, 2002: Self-organizing feature maps predicting sea levels. *Info. Sci.,* **144,** 91–125.

Vesanto, J., J. Himberg, E. Alhoniemi, and J. Parhankangas, 2000: SOM toolbox for Matlab 5. Helsinki University of Technology, Finland. [Available online at http://www.cis.hut.fi/projects/somtoolbox/.]

Weare, B. C., A. R. Navato, and R. E. Newell, 1976: Empirical orthogonal analysis of Pacific sea surface temperature. *J. Phys. Oceanogr.,* **6,** 671–678.

Weisberg, R. H., and R. He, 2003: Local and deep-ocean forcing contributions to anomalous water properties on the West Florida Shelf. *J. Geophys. Res.,* **108,** 3184, doi:10.1029/2002JC001407.

——, B. Black, and H. Yang, 1996: Seasonal modulation of the west Florida shelf circulation. *Geophys. Res. Lett.,* **23,** 2247–2250.

——, R. He, G. Kirkpatrick, F. Muller-Karger, and J. J. Walsh, 2004: Coastal ocean circulation influences on remotely sensed optical properties: A West Florida Shelf case study. *Oceanography,* **17** (2), 68–75.